

Article

EPR Spectroscopy of Cu(II) Complexes: Prediction of g -Tensors Using Double-Hybrid Density Functional Theory

Maria Drosou ^{1,*}, Christiana A. Mitsopoulou ¹, Maylis Orio ² and Dimitrios A. Pantazis ^{3,*}

¹ Inorganic Chemistry Laboratory, National and Kapodistrian University of Athens, Panepistimiopolis, 15771 Zografou, Greece; cmitsop@chem.uoa.gr

² CNRS, Aix-Marseille Université, Centrale Marseille, iSm2, 13013 Marseille, France; maylis.orio@univ-amu.fr

³ Max-Planck-Institut für Kohlenforschung, Kaiser-Wilhelm-Platz 1, 45470 Mulheim an der Ruhr, Germany

* Correspondence: mdrosou@chem.uoa.gr (M.D.); dimitrios.pantazis@kofo.mpg.de (D.A.P.)

Abstract: Computational electron paramagnetic resonance (EPR) spectroscopy is an important field of applied quantum chemistry that contributes greatly to connecting spectroscopic observations with the fundamental description of electronic structure for open-shell molecules. However, not all EPR parameters can be predicted accurately and reliably for all chemical systems. Among transition metal ions, Cu(II) centers in inorganic chemistry and biology, and their associated EPR properties such as hyperfine coupling and g -tensors, pose exceptional difficulties for all levels of quantum chemistry. In the present work, we approach the problem of Cu(II) g -tensor calculations using double-hybrid density functional theory (DHDFT). Using a reference set of 18 structurally and spectroscopically characterized Cu(II) complexes, we evaluate a wide range of modern double-hybrid density functionals (DHDFs) that have not been applied previously to this problem. Our results suggest that the current generation of DHDFs consistently and systematically outperform other computational approaches. The B2GP-PLYP and PBE0-DH functionals are singled out as the best DHDFs on average for the prediction of Cu(II) g -tensors. The performance of the different functionals is discussed and suggestions are made for practical applications and future methodological developments.

Keywords: copper; g -tensors; density functional theory; double-hybrid functionals; theoretical spectroscopy



Citation: Drosou, M.; Mitsopoulou, C.A.; Orio, M.; Pantazis, D.A. EPR Spectroscopy of Cu(II) Complexes: Prediction of g -Tensors Using Double-Hybrid Density Functional Theory. *Magnetochemistry* **2022**, *8*, 36. <https://doi.org/10.3390/magnetochemistry8040036>

Academic Editors: Dinar Abdullin and Angeliki Giannoulis

Received: 19 February 2022

Accepted: 19 March 2022

Published: 23 March 2022

Publisher's Note: MDPI stays neutral with regard to jurisdictional claims in published maps and institutional affiliations.



Copyright: © 2022 by the authors. Licensee MDPI, Basel, Switzerland. This article is an open access article distributed under the terms and conditions of the Creative Commons Attribution (CC BY) license (<https://creativecommons.org/licenses/by/4.0/>).

1. Introduction

Copper is among the most abundant transition metals in bioinorganic systems [1–7]. Electron paramagnetic resonance (EPR) spectroscopy is a uniquely useful approach for Cu(II) systems because it provides direct insights into the electronic and geometric structure of Cu(II) centers and the nature of their ligand sphere [4,8]. Relationships between structure and EPR parameters have been previously discussed based on ligand-field theory, as well as experimental correlations [8–13]. However, such correlations are often hard to extend to complex structural cases such as those frequently encountered in enzymatic active sites. Therefore, in most cases, interpretation of EPR spectroscopy requires input from quantum chemical calculations that correlate expected EPR parameters with molecular electronic and geometric structure [14–24]. A primary target property for Cu(II) systems is the g -matrix (commonly referred to as g -tensor), which describes the interaction of the unpaired electron with the effective magnetic field. The limitations of classical density functional theory (DFT) methods to accurately predict g -tensors of copper systems have been recognized in multiple studies [20,21,25–30] and have been attributed to deficiencies in the description of the covalency of Cu–ligand bonds [29,31] and of the electronic excitation energies [29]. Notably, wavefunction-based methods, although systematically improvable and able to achieve arbitrary levels of accuracy, cannot at this point in time be applied to copper-based systems without the introduction of approximations that are detrimental for the accuracy of the predicted parameters [25,32–35], as well as for hyperfine coupling constants [36], thus severely restricting the utility of these methods. Hence, density functional theory

(DFT) currently provides the best compromise between accuracy and cost and serves as the most promising and pragmatic platform for establishing practically useful computational protocols with predictive value.

Over the last thirty years, a plethora of density functionals (DFs) has been developed [37,38], with different levels of approximation and empirical parameters optimized for the prediction of different chemical properties. Notably, EPR parameters practically never feature in training sets of new DFs. Experience shows that local density approximation (LDA)- and generalized-gradient approximation (GGA)-type functionals systematically underestimate g -values [20,21]. Hybrid density functionals (HDFs) include a Hartree–Fock (HF) exchange component (also called exact exchange, EEX). Inclusion of this exchange term in common hybrid functionals is beneficial [20,21,28,30], but standard HDFs still cannot provide sufficient accuracy. Increasing the admixture of exact exchange (EEX) to 30–40% has been recognized as a good strategy to improve the accuracy of g -tensor calculations for 3d, 4d and 5d transition metal complexes [39–42], while the effect of changing the correlation functional is minimal in comparison. However, increasing the Hartree–Fock exchange percentage introduces spin contamination in unrestricted calculations [43], which may be detrimental for SOMOs that have metal-ligand antibonding character. Local hybrid functionals with position-dependent EEX admixture have been reported to alleviate the problem of spin polarization [44].

Double-hybrid density functionals (DHDFs) additionally introduce unoccupied Kohn–Sham orbitals via perturbation theory. Several benchmark studies have confirmed the superior performance on DHDFs on a wide range of properties, such as relative energies, thermochemistry and electronic excitation energies [45–47]. Based on the general idea that “pure” DFT functionals allow a better description of static correlation at the expense of dynamic correlation effects [48–50], and MP2 contributes a better description of dynamic correlation [45], the judicious combination of the two is expected to achieve a good balance of dynamic and non-dynamic correlation effects. DHDFs have exhibited excellent performance on response properties calculations, such as g -tensors of organic radicals [51], electric field response properties of water nanoclusters [52], hyperfine coupling constants [53,54] and NMR nuclear shielding constants [55]. However, their performance for g -tensors of transition metal systems in general and for the particularly demanding case of Cu(II) in particular remains unexplored. To determine the scope of applicability of these approximations for the title problem, in this study we investigate the performance of sixteen distinct DHDFs for the prediction of g -tensors of a reference set of eighteen Cu(II) complexes with experimentally known structures and EPR parameters. The performance of DHDFs is contrasted with the best performing hybrid functionals for g -tensor prediction for Cu(II) complexes as reported by a recent benchmark study by Sciortino et al. [26]. Based on our results, we establish that most of the recent DHDFs outperform standard global HDFs and we are able to suggest specific DHDF-based protocols that maximize the accuracy for g -tensor calculations of copper-based enzymes.

2. Methodology

2.1. Benchmark Set of Copper Complexes

The structures of the eighteen Cu(II) complexes selected for the present study are shown in Figure 1. The set includes ligands with N, O and S coordinating atoms in different combinations. Similar sets of Cu(II) complexes have been employed in previous benchmarking studies [25–27,36]. The complexes are approximately square planar, except **9** and **12**, which are square pyramidal, and **18**, which is octahedral.

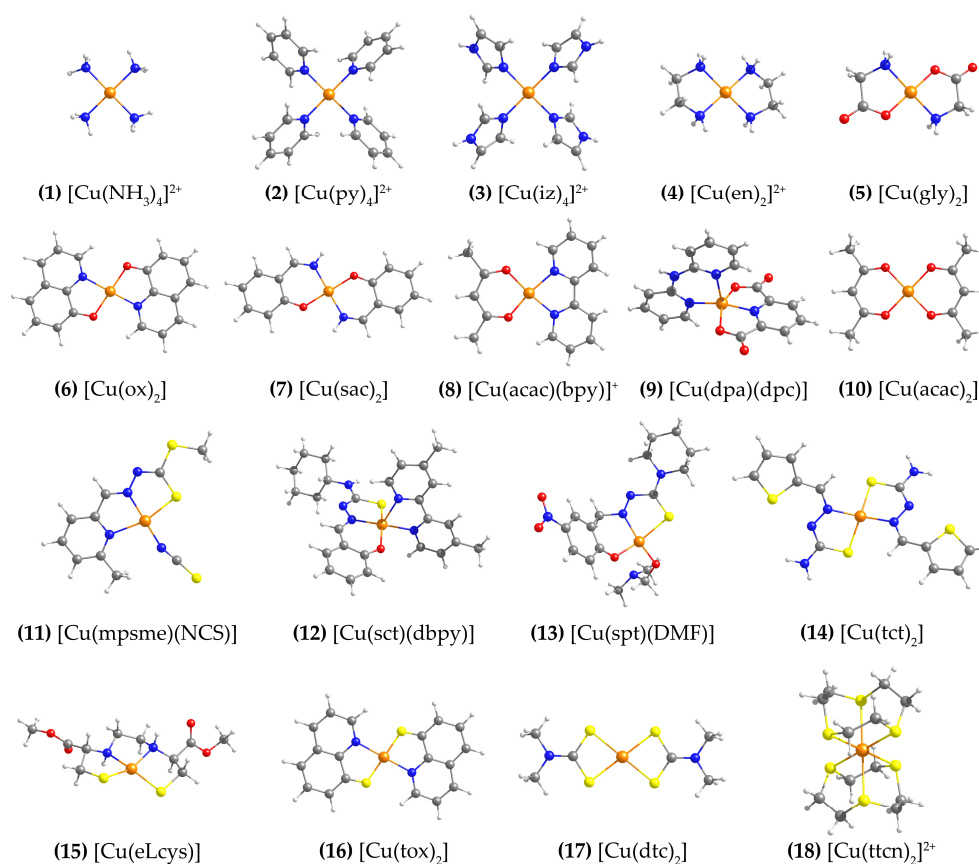


Figure 1. Structures of the eighteen Cu(II) complexes studied in this work. Ligand abbreviations: py = pyridine; iz = imidazole; en = ethylenediamine; gly = glycine; ox = 3-quinolinolato; sac = salicylaldehyde imine; acac = acetylacetonate; bpy = 2,2'-bipyridine; dpa = 2,2'-dipyridylamine; dpc = dipicolinate ligand; mpsme = anionic form of the 6-methyl-2-formylpyridine Schiff base of S-methyldithiocarbamate; sct = N(4)-cyclohexyl thiosemicarbazone; dbpy = 4,4'-dimethyl-2,2'-bipyridine; spt = 5-nitrosalicylaldehyde piperidylthiosemicarbazone; tct = thiophene-2-carbaldehyde thiosemicarbazone; DMF = N,N-Dimethylformamide; eLcys = N,N'-ethylenbis(L-cysteine); tox = 3-quinolinethiolato; dtc = dimethyl-dithiocarbamate, ttcn = 1,4,7-trithiacyclononane.

It is noted that the g -tensor is expressed as:

$$\mathbf{g} = g_e \mathbf{I} + \Delta \mathbf{g} \quad (1)$$

where each component Δg_{xx} , Δg_{yy} , Δg_{zz} describes the shift of the system's g -value from the g -value of the free electron ($g_e = 2.002319$) and \mathbf{I} is the identity matrix. In this work, we express the principal components of the g -tensors as g -shifts in parts per thousand (ppt), computed as $\Delta g = (g - g_e) \cdot 1000$. The largest component is referred to as Δg_{zz} or as the parallel g -tensor component, Δg_{\parallel} . We define the perpendicular g -tensor component as the average of the two smaller components: $\Delta g_{\perp} = (\Delta g_{xx} + \Delta g_{yy})/2$.

The g -tensor components of complexes 1–18 have been experimentally determined from EPR measurements and are given in Table 1. Since Cu(II) complexes have a d^9 configuration, square planar and square pyramidal structures usually exhibit strongly axial EPR signals, i.e., $\Delta g_{xx} < \Delta g_{yy} \ll \Delta g_{zz}$, consistent with the high $d_{x^2-y^2}$ character of the singly occupied molecular orbital (SOMO). The g -shifts arise predominantly due to the interaction of the ligating atoms with the unpaired electron, so it depends on the nature of the ligands, the nature of the Cu–ligand bond, and the corresponding bond lengths. In this benchmark set we include complexes with variable coordination spheres and a wide range of Δg_{zz} values, from 83 ppt to 283 ppt. The presence of at least one S atom on the

copper coordination sphere decreases the magnitude of Δg_{zz} . It should be noted that mixed ligand complexes exhibit magnetic parameters that are intermediate between the respective complexes with four of the same ligands of each type [8]. This pattern can be observed in the experimental data shown in Table 1.

Table 1. Experimental Δg values (ppt) of the Cu(II) complexes 1–18 studied in this work. Molecular structures of the complexes are shown in Figure 1. The complexes are arranged in groups according to the copper-coordinating atoms for each subgroup, which are also shown for convenience.

	Complex	Coord. Core	Δg_{xx}	Δg_{yy}	Δg_{zz}	Ref.
1	[Cu(NH ₃) ₄] ²⁺	N4	45	45	239	[56]
2	[Cu(py) ₄] ²⁺		51	51	261	[56]
3	[Cu(iz) ₄] ²⁺		45	45	260	[56]
4	[Cu(en) ₂] ²⁺		39	39	203	[56]
5	[Cu(gly) ₂]	N2O2	50	50	265	[56]
6	[Cu(ox) ₂]		50	50	200	[57]
7	[Cu(sac) ₂]		48	48	238	[58]
8	[Cu(acac)(bpy)] ⁺		48	55	251	[59]
9	[Cu(dpa)(dpc)]	N3O2	60	60	252	[60]
10	[Cu(acac) ₂]	O4	58	58	283	[61]
11	[Cu(mpsme)(NCS)]	N3S	48	48	203	[62]
12	[Cu(sct)(dbpy)]	N3OS	54	54	165	[63]
13	[Cu(spt)(DMF)]	NO2S	35	46	201	[64]
14	[Cu(tct) ₂]	N2S2	27	88	112	[65]
15	[Cu(eLcys)]		37	37	124	[66]
16	[Cu(tox) ₂]		42	42	136	[57]
17	[Cu(dtc) ₂]	S4	23	23	83	[67]
18	[Cu(ttcn) ₂] ²⁺	S8	25	25	112	[68]

2.2. Overview of Double Hybrid Density Functionals

In double-hybrid density functional theory, a set of Kohn–Sham orbitals is first obtained by a classical HDFT calculation. Subsequently, an MP2 calculation is performed based on this set of orbitals. A general expression for the total exchange–correlation term for standard DHDFs is:

$$E_{XC}^{DHDF} = c_X E_X^{HF} + (1 - c_X) E_X^{DFT} + c_C^{DFT} E_C^{DFT} + c_C^{MP2} E_S^{MP2} \quad (2)$$

where c_X is the amount of DFT exchange, and c_C^{DFT} and c_C^{MP2} are the amounts of DFT and MP2 correlation, respectively. Usually, but not always, $c_C^{MP2} = 1 - c_C^{DFT}$. The parameters c for all functionals studied in this work are shown in Table 2. The first DHDF was B2PLYP [47], proposed by Grimme and parametrized in order to reproduce heats of formation. The success of B2PLYP inspired further developments. mPW2PLYP [69] has a modified exchange part and higher accuracy towards the calculation of thermodynamic properties and barrier heights. B2GP-PLYP [70] has increased amounts of exact exchange and perturbative correlation, suggested for general purpose (GP) applications. B2K-PLYP and B2T-PLYP [71] were parametrized for reaction kinetics and thermochemistry. Some researchers attempted to minimize or eliminate the use of empirically defined parameters, striving instead to include parameters that have theoretical justification. Such functionals include PBE-QIDH [72], PBE0-DH [73] and the range-separated RSX-QIDH [74] and RSX-0DH [75], optimized by enforcing reproduction of the total energy of the hydrogen atom.

Table 2. Parameters of DHDFs according to Equations (2)–(4).

Functional	c_X	μ	c_C^{DFT}	c_C^{MP2}	c_O	c_S
B2PLYP	0.53	-	0.73	0.27	-	-
mPW2PLYP	0.55	-	0.75	0.25	-	-
B2GP-PLYP	0.65	-	0.64	0.36	-	-
B2K-PLYP	0.72	-	0.58	0.42	-	-
B2T-PLYP	0.60	-	0.69	0.31	-	-
PBE-QIDH	0.69	-	0.67	0.33	-	-
PBE0-DH	0.50	-	0.875	0.125	-	-
DSD-BLYP	0.75	-	0.53	-	0.46	0.60
DSD-PBEP86	0.72	-	0.44	-	0.51	0.36
ω B2PLYP	0.53	0.30	0.73	0.27	-	-
ω B2GP-PLYP	0.65	0.27	0.64	0.36	-	-
RSX-QIDH	0.69	0.27	0.67	0.33	-	-
RSX-ODH	0.50	0.33	0.875	0.125	-	-
ω B88PP86	0.65	0.20	0.58	0.42	-	-
ω PBEP86	0.70	0.18	0.68	0.48	-	-
ω B97X-2	0.63(6)	0.30	1.00	1.00	0.44(7)	0.52(9)

As a variation of the standard MP2 approach, some functionals may treat the same-spin and opposite-spin correlation contributions separately and with unequal weights. This is referred to as a spin-component scaling (SCS). In case the same-spin contribution is entirely omitted, the approach is referred to as spin-opposite scaled (SOS). The general expression for the total exchange-correlation term for the spin-component scaled double-hybrid functionals with dispersion correction (DSD-DFT) is:

$$E_{XC}^{\text{DSD-DHDF}} = c_X E_X^{\text{HF}} + (1 - c_X) E_X^{\text{DFT}} + c_C E_C^{\text{DFT}} + c_O E_O^{\text{MP2}} + c_S E_S^{\text{MP2}} + s_6 E_D \quad (3)$$

where c_O is the amount of opposite-spin MP2, c_S of same-spin MP2, and s_6 of the dispersion correction. DSD-BLYP [76] and DSD-PBEP86 [77] have been parametrized to reproduce thermochemistry, kinetics, and dispersion forces, and were found to be more accurate than the previously most successful B2GP-PLYP functional.

In range-separated DFs [78–80], the interelectronic repulsion, r_{12}^{-1} , is separated using an error function, erf, into a short-range and a long-range component:

$$\frac{1}{r_{12}} = \frac{1 - [|\alpha + \beta \cdot \text{erf}(\mu \cdot r_{12})|]}{r_{12}} + \frac{\alpha + \beta \cdot \text{erf}(\mu \cdot r_{12})}{r_{12}} \quad (4)$$

where the first term accounts for the short-range interaction and the second term accounts for the long-range interaction. ω B2PLYP and ω B2GP-PLYP [81] functionals were parametrized to reproduce electronic excitation energies. In addition, ω B88PP86 and ω PBEP86 [82] were very recently presented, parametrized to reproduce experimental singlet-singlet as well as singlet-triplet excitations. The first range-separated DHDF that also includes spin component scaling, ω B97X-2 [83], was parametrized for thermochemistry, kinetics, and noncovalent interactions. The parameters μ from Equation (4) for the range separated functionals used herein are shown in Table 2.

3. Results and Discussion

3.1. Evaluation Criteria

Evaluation of the methods used for the prediction of the g -shifts was based on the differences (D) of the calculated from the experimental parallel and perpendicular components:

$$D(\Delta g_{\parallel}) = \Delta g_{zz}^{\text{calc}} - \Delta g_{zz}^{\text{exp}} \quad (5)$$

$$D(\Delta g_{\perp}) = \frac{\Delta g_{xx}^{\text{calc}} + \Delta g_{yy}^{\text{calc}}}{2} - \frac{\Delta g_{xx}^{\text{exp}} + \Delta g_{yy}^{\text{exp}}}{2} \quad (6)$$

The mean values of the above parameters for each function for the set of eighteen Cu(II) complexes under study are used to describe the performance of the functional. The mean absolute difference (MAD) of the Δg_{\parallel} component is defined as:

$$\text{MAD}(\Delta g_{\parallel}) = \frac{1}{N} \cdot \sum_{i=1}^N |D(\Delta g_{\parallel})_i| \quad (7)$$

and straightforwardly describes the ability of the method to reproduce the experimental values, while the mean difference (MD) reflects the possible *systematic* over- or under-estimation of g -shifts by the specific method.

The standard deviation of the above parameters was also considered. The standard deviation of the differences (SDD) is estimated as:

$$\text{SDD}(\Delta g) = \sqrt{\frac{1}{N} \cdot \sum_{i=1}^N [D(\Delta g)_i - \text{MD}(\Delta g)]^2} \quad (8)$$

and the standard deviation of the absolute differences (SDAD):

$$\text{SDAD}(\Delta g) = \sqrt{\frac{1}{N} \cdot \sum_{i=1}^N [|D(\Delta g)_i| - \text{MAD}(\Delta g)]^2} \quad (9)$$

Finally, the mean absolute percentage differences (MAPD) are examined:

$$\text{MAPD}(\Delta g) = \frac{1}{N} \cdot \sum_{i=1}^N \frac{|D(\Delta g)_i|}{\Delta g_i^{\text{exp}}} \cdot 100 \quad (10)$$

3.2. Performance of Functionals

The mean values of the evaluation criteria for each functional are shown in Table 3. To begin with, we observe that the MAPDs for Δg_{\perp} are very close to those for Δg_{\parallel} , therefore we focus our analysis on the parallel components for simplicity and the conclusions largely reflect also the performance for the perpendicular components of the g -tensor. Besides, since the parallel component is the largest, it also has the largest D values. We start the evaluation of the relative performances by examining the MADs and MDs. The $\text{MAD}(\Delta g_{\parallel})$ and $\text{MD}(\Delta g_{\parallel})$ values for the 19 functionals are plotted in Figure 2, top. Complete results are provided in the Supporting Information, Tables S1–S19.

Focusing first on conventional hybrid functionals, we see that B3LYP is the worst method considered here. It shows the largest $\text{MAD}(\Delta g_{\parallel})$ value of 67 ppt, while PBE0 and BHandHLYP follow with $\text{MAD}(\Delta g_{\parallel})$ values of 54 and 48 ppt, respectively. Thus, among conventional HDFs the best performance is observed for PBE0 and BHandHLYP, which is in agreement with Sciortino et al. [26]. Only two double-hybrid functionals perform similarly to HDFs. These are B2PLYP and RSX-QIDH with $\text{MAD}(\Delta g_{\parallel})$ values of 57 and 55 ppt, respectively. Figure 2 top suggests that apart from the B2PLYP and RSX-QIDH, all remaining 14 DHDFs outperform HDFs and show similar performance in terms of the MADs, but have different MDs, which means that they show different systematic behaviour. The $\text{MAD}(\Delta g_{\parallel})$ of the other 14 functionals range between 31 and 42 ppt. The lowest $\text{MAD}(\Delta g_{\parallel})$ is 31 ppt, achieved by the B2GP-PLYP and PBE0-DH functionals. The ω B2GP-PLYP, ω B88PP86 and ω PBEP86 follow with MADs of 32, 33 and 34 ppt, respectively. The lowest $\text{MD}(\Delta g_{\parallel})$ values among the DHDFs are observed for the PBE0-DH and ω B88PP86 functionals at -7 and -9 ppt, respectively. Notably, apart from the MAD and MD values, the respective SDs must be also considered. The differences between the individual $D(\Delta g_{\parallel})_i$ values of the complexes **1–18**, visualized in Figure 2 bottom, reflect the error of each method on reproducing the relative Δg_{\parallel} values of the various structures.

They are also described by the SDD value of each method, given in Table 3. ω B2GP-PLYP, ω PBEPP86 and ω B88PP86 have larger SD values than the B2GP-PLYP and PBE0-DH functionals, which means that there is a larger spread of D values with these functionals.

Table 3. Mean difference (MD) and standard deviation of the differences (SDD), mean absolute difference (MAD), standard deviation of the absolute differences (SDAD) and mean absolute percent difference (MAPD), from the experimental values of the parallel and perpendicular g -shifts components calculated with each functional. Values are expressed in ppt.

Functional	MD (Δg_{\parallel})	SDD (Δg_{\parallel})	MAD (Δg_{\perp})	MAD (Δg_{\parallel})	SDAD (Δg_{\parallel})	MAPD (Δg_{\perp})	MAPD (Δg_{\parallel})
PBE0	−49	41	6	54	35	14	24
BHandHLYP	36	49	19	48	38	49	35
B3LYP	−66	41	9	67	40	19	30
B2PLYP	−57	28	12	57	28	31	30
mPW2PLYP	−38	30	8	42	24	19	21
B2GP-PLYP	−10	34	7	31	16	18	18
B2K-PLYP	25	41	8	37	31	21	24
B2T-PLYP	−27	31	7	36	20	19	19
PBE-QIDH	31	41	10	40	32	25	27
PBE0-DH	−9	35	6	31	19	15	17
DSD-BLYP	28	43	8	39	34	21	25
DSD-PBEP86	21	43	7	37	30	20	24
ω B2PLYP	−19	33	6	34	18	17	18
ω B2GP-PLYP	14	37	7	32	24	19	21
RSX-QIDH	53	46	15	55	44	37	39
RSX-0DH	26	43	14	40	31	35	28
ω B88PP86	−7	36	7	33	17	19	19
ω PBEPP86	10	40	7	34	23	20	21
ω B97X-2	−16	39	7	38	20	19	20

Inspection of the individual $D(\Delta g_{\parallel})_i$ values for the complexes 1–18 obtained with each functional allows a more in-depth analysis of our results (Figure 2 bottom). This diagram shows clearly that complexes 11–18, which have at least one S coordinated ligand on copper, are described differently than complexes 1–10, which have only N and O ligating atoms. Specifically, most functionals underestimate the value of parallel g -tensor component of structures 1–10, while they overestimate it for 11–18. This behavior is even more pronounced for the HDFs. Figure 2 bottom shows clearly that even though DHDFs also treat differently the Cu–S bond, they not only have smaller MADs, but also the spread of the Δg_{\parallel} values is smaller. This implies that DHDFs achieve a more balanced description of Cu–ligand bond covalency and this behavior is transferable among different systems, at least to a larger extent than HDFs.

In Figure 3, the $D(\Delta g_{\parallel})$ obtained by each functional is plotted against the calculated copper Löwdin spin population of the MP2 relaxed density, $\rho_s(\text{Cu})$, for six complexes chosen as representative of different copper coordination spheres, i.e., N4, N2O2, O4, N2S2, N3OS and S4 (see Figure S1 for additional examples). Several conclusions can be extracted from these diagrams. First, it can be clearly observed that the value of $D(\Delta g_{\parallel})$ increases following a near linear trend along with $\rho_s(\text{Cu})$. Second, each system has a different $\rho_s(\text{Cu})$ value for which the experimental Δg_{\parallel} is reproduced. Even though no single functional predicts this most favorable $\rho_s(\text{Cu})$ value for all complexes, structures with similar coordination spheres are optimally described by the same density functionals (Figure S1). Among the DHDFs included in this study, the B2PLYP and RSX-QIDH predict the smallest and largest $\rho_s(\text{Cu})$ values, respectively, for all complexes, which directly correlates with the observed systematic negative and positive differences from the experimental values, reflected in the large MD(Δg_{\parallel}) values shown in Figure 3. In addition, B3LYP and PBE0 in almost all cases predict a small spin population on Cu. Notably, accurate g -tensor prediction does not necessarily imply prediction of the “correct” spin density, since other factors, such as

higher order relativistic contributions, could also alter the $D(\Delta g_{\parallel})$ values. We note that the possible lack of correspondence between the accuracy of DFs in the prediction of various observable properties, such as relative energies or ionization potentials, and the quality of the computed densities has been extensively debated recently [84–86].

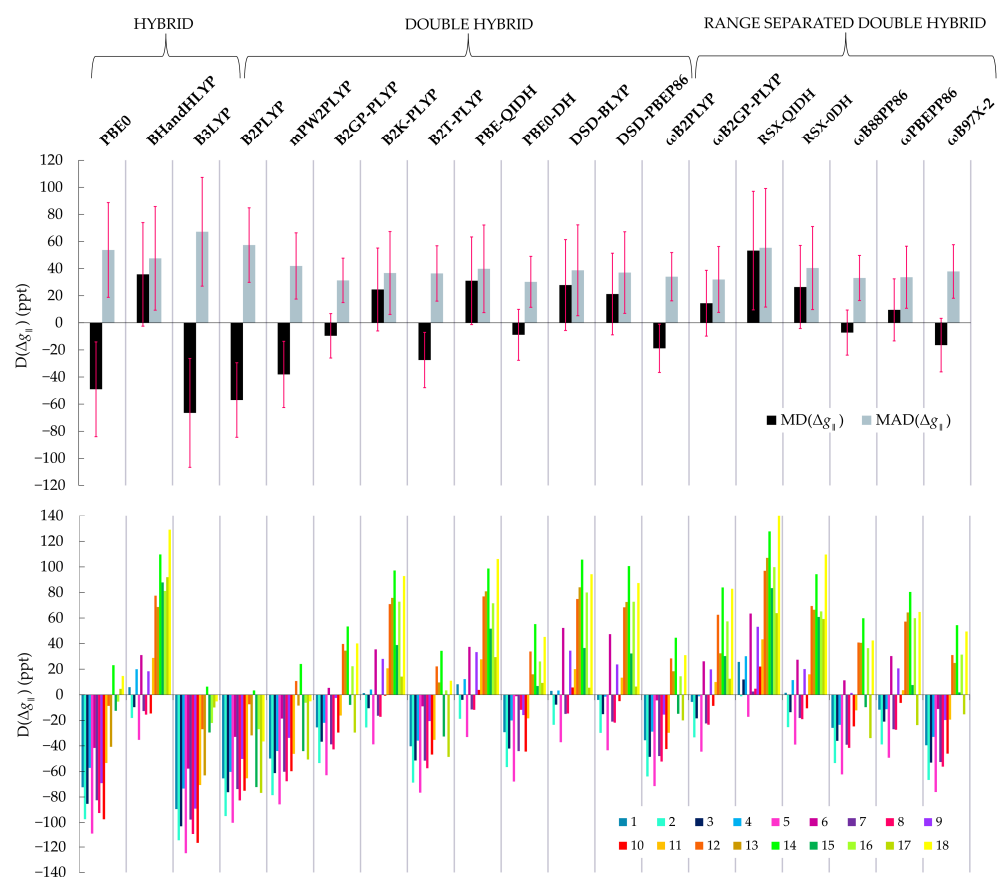


Figure 2. (Top): Mean absolute difference (MAD), mean difference (MD) from the experimental values of the parallel g -tensor component calculated with each functional. The respective standard deviations (SD) are plotted in pink. (Bottom): Differences (D) from the experimental values of the parallel g -tensor component of each one of the 18 Cu(II) complexes of the set calculated with each functional. Each bar color represents a complex.

From the above analysis we can see that overall, the best performing functionals for this set of Cu(II) complexes are the B2GP-PLYP and PBE0-DH, because they have both the lowest $MAD(\Delta g_{\parallel})$ values, and at the same time among the lowest $MD(\Delta g_{\parallel})$ and SD values. PBE0-DH represents a definite improvement over the parent PBE0 functional, which is the best performing HDF. Interestingly, these two DHDFs represent different construction philosophies (PBE0-DH is “non empirical”) yet converge to similarly accurate behavior. Notably, even though the parameters of B2GP-PLYP (and B2PLYP) were empirically optimized, they were also suggested to be justified from a purely theoretical standpoint [87]. It is also important to draw attention to the observation that the functionals ω B2PLYP, ω B88PP86, ω B2GP-PLYP, ω PBEP86 are among the best performing DHDFs. What these functionals have in common is that they were parametrized to reproduce experimental excitation energy reference values [81,82].

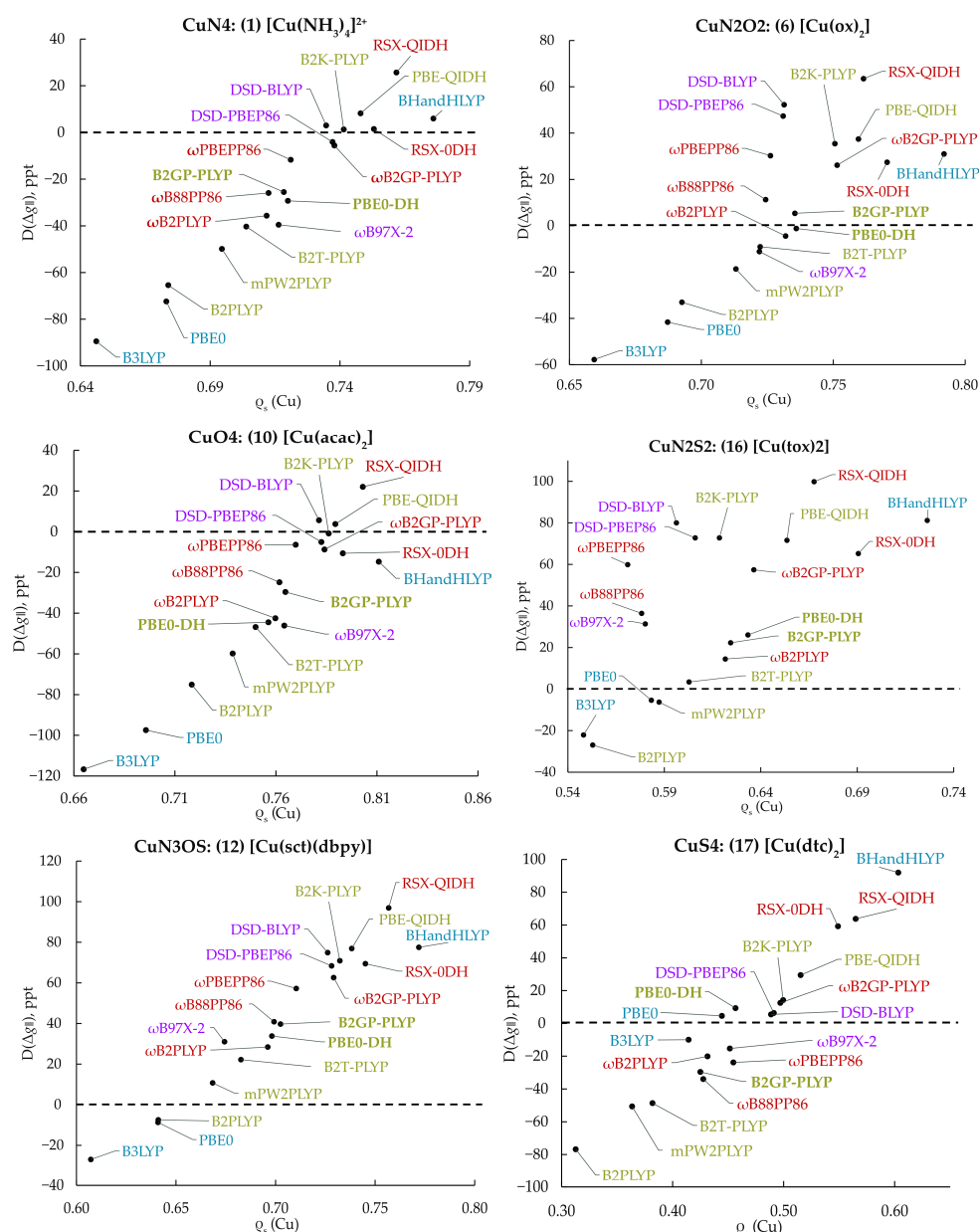


Figure 3. Correlation of the differences, $D(\Delta g_{||})$, of the calculated g -tensor from the experimental value of the parallel g -shift with the Cu spin populations computed with the respective functional for complexes 1, 6, 10, 16, 12 and 17, which have different copper coordination spheres.

Another interesting point concerns the calculated SDD values in Table 3. These show that the B2PLYP functional has the smallest SDD value of 28 ppt. This is visually represented in Figure 2b, where it can be observed that even though B2PLYP performs poorly, systematically underestimating the g -shifts, its behavior is distinct in that the D values of complexes 11–18 with S coordinating ligands are not very different from complexes 1–10 which have N and O ligands only. By contrast, this is not observed for RSX-QIDH, the other DHDF of this set that performs poorly, systematically overestimating g -shifts. Therefore, we can conclude that B2PLYP achieves a more balanced description of the Cu-ligand bond covalency between different ligand donors.

Having compared the relative accuracies of the examined DHDFs on predicting the experimental g -tensor components, one may consider whether correlations exist between their construction parameters (Table 2) and their performance. However, at this point it is not possible to discern any obvious correlation. Perhaps a way to approach this

problem is to investigate how reference spin densities, computed with high-level ab initio methods, are reproduced by density functionals with respect to the parameters included in their definition [86]. Although clear choices emerge from the present study for practical applications, further systematic studies are required for the development of improved functionals optimized for spin-density dependent properties.

4. Conclusions

We investigated the performance of sixteen DHDF approximations for the prediction of experimental g -shifts of a set of eighteen Cu(II) complexes. The DHDFs results were compared with the best performing HDFs for Cu(II) complexes [26]. Our results show that most DHDFs perform significantly better than the best performing standard HDFs, establishing a new standard for the prediction of g -tensors of copper systems. With the exception of B2PLYP and RSX-QIDH, all other DHDFs perform significantly better than HDFs. Based on the criteria defined in Section 3.1, we found that the ranking of the DHDFs with respect to g -tensor prediction is: B2GP-PLYP \sim PBE0-DH $>$ ω B2PLYP \sim ω B88PP86 $>$ B2T-PLYP \sim ω B2GP-PLYP \sim ω PBEP86 $>$ B2K-PLYP \sim PBE-QIDH \sim DSD-BLYP \sim DSD-PBEP86 \sim RSX-0DH \sim ω B97X-2 $>$ mPW2PLYP $>$ B2PLYP $>$ RSX-QIDH.

The best-performing functionals represent different approaches toward construction of DHDFs. B2GP-PLYP is a general purpose empirically fitted functional based on B2PLYP, while PBE0-DH is based on PBE0 and obtained by purely theoretical arguments. Nevertheless, they converge to similarly good performance. Moreover, the equally good performance of the range-separated ω B2PLYP, ω B88PP86, ω B2GP-PLYP and ω PBEP86 directs our attention to functionals optimized for excitation energies. We suggest that such functionals can be used as a starting point for further refinement, taking into account a more extensive set of transition metal reference compounds for g -tensors, and perhaps also for other spin-dependent properties.

Overall, the double-hybrid methodologies significantly outperform conventional hybrid approaches, offering a good balance between accuracy and computational cost. We note that due to the steep scaling of MP2 ($O(N^5)$ where N is a measure of the system size), the computational cost of DHDFs on large (>100 atoms) systems increases more steeply than HDFs in terms of both time and required memory. Hence, for large systems we propose the use of multilevel approaches, where the metal and first coordination sphere ligands are treated with a DHDF method and the surrounding protein matrix can be treated with a cheaper DFT method. Based on our results, we recommend the use of B2GP-PLYP and PBE0-DH functionals for g -tensor calculations on Cu(II) complexes bearing N, O and S ligands, which are usually encountered in bioinorganic systems. Evidently, the uncertainty of even the best functionals may exceed the uncertainty of experimental values. This suggests that the successful use of these approaches will depend on the type of chemical problem under investigation and in the combination with complementary data. Nevertheless, the present study clearly defines the current state-of-the-art in quantum chemical calculations of g -tensors for Cu(II) systems and encourages further developments in refining double-hybrid DFT for spin density dependent properties.

5. Computational Details

All calculations were performed with Orca 5 [88]. Geometry optimizations of the eighteen Cu(II) complexes of the benchmark set was performed with the B3LYP [89–91] functional, starting from the crystallographic structures obtained from the Cambridge Structural database [92]. Scalar relativistic effects were treated using the zeroth-order regular approximation (ZORA) [93,94]. The resolution of identity (RI) approximation [95] and the chain-of-spheres approximation to exact exchange (COSX) [96] were used throughout to reduce computational time. Tight convergence criteria and high-quality grids (DefGrid3 in Orca convention) were used throughout. The ZORA-recontracted [97] version of the def2-TZVPP basis set [98] was used for Cu and the ZORA-def2-TZVP for all other atoms, along with fully decontracted def2/J auxiliary basis sets [99]. Since MP2 convergence with

basis set size can be slower than DFT, the basis set dependence of DHDFs may increase with increasing fraction of the PT2 component [46,47]. To investigate the dependence of calculated g -shifts on the basis set size, we carried out systematic studies on complexes **3**, **10** and **17**, which have N₄, O₄ and S₄ coordination spheres, respectively, using the B2PLYP and DSD-PBEP86 functionals. In line with previous studies on Cu(II) g -tensor calculations [25], the dependence on the basis set is very weak past the polarized triple-zeta level and the use of the largest available ZORA-def2-QZVPP basis set leads to negligible differences (of the order of 1–2 ppt) in the results compared to the triple-zeta basis sets. The maximum difference in computed g -shifts upon use of the quadruple-zeta basis set (5 ppt) was observed for **17** with the DSD-PBEP86 functional. Since this difference is of the same order of magnitude as the experimental uncertainty, the basis sets used here are judged to be essentially converged for all practical purposes. For the calculation of g -tensors, the DFT functionals tested in this work are: the hybrid functionals PBE0 [100–102], BHandHLYP [91], B3LYP [89–91], the double-hybrid functionals: B2PLYP [47], mPW2PLYP [69], B2GP-PLYP [70], B2K-PLYP [71], B2T-PLYP [71], PBE-QIDH [72], PBE0-DH [73], DSD-BLYP [76], DSD-PBEP86 [77], and the range-separated double-hybrid functionals: ω B2PLYP [81], ω B2GP-PLYP [81], RSX-QIDH [74], RSX-0DH [75], ω B88PP86 [82], ω PBEP86 [82], ω B97X-2 [83]. Spin contamination values for HDFs were smaller than 0.01 for all complexes, which suggests that the ground state of all complexes can be adequately described by a single determinant. For the calculations with double-hybrid functionals the NoFrozenCore option was used. In terms of computational costs, we mention as an example that for complexes **1** (17 atoms), **18** (43 atoms) and **12** (63 atoms) the PBE0 calculation needs 1, 16 and 48 min, respectively, using 10 processing cores, while the PBE0-DH calculation needs 3, 184 and 927 min, respectively. The part of the calculation that is responsible for most of the additional computational effort is the calculation of the relaxed MP2 response density, which incorporates orbital relaxation and is consistent with first order properties as analytic derivatives. The spin-orbit coupling was treated using the spin-orbit mean-field (SOMF) operator [102] with the 1X-approximation [103,104] (SOCType 3 in ORCA convention). For the construction of the potential one-electron terms were included, the Coulomb term was computed using the RI approximation, exchange terms were incorporated via one-center exact integrals including the spin-other orbit interaction, and without local DFT correlation terms (SOCFlags 1,3,3,0 in ORCA). Picture change effects were also taken into account.

Supplementary Materials: The following supporting information can be downloaded at: <https://www.mdpi.com/article/10.3390/magnetochemistry8040036/s1>, Figure S1: Correlation of the differences, $D(\Delta g_{\parallel})$, of the calculated g -tensor from the experimental value of the parallel g -shift with the Cu spin populations computed with the respective functional for pairs of complexes with the same copper-coordinating atoms **1** and **3**, **14** and **16**, and with similar coordination spheres **12** and **13**. Tables S1–S19: Detailed results for each functional.

Author Contributions: Conceptualization, D.A.P. and M.D.; methodology, D.A.P. and M.D.; formal analysis, M.D., D.A.P. and M.O.; investigation, M.D.; data curation, M.D.; writing—original draft preparation, M.D.; writing—review and editing, D.A.P. and M.D.; supervision, C.A.M.; project administration, D.A.P., C.A.M. and M.O.; All authors have read and agreed to the published version of the manuscript.

Funding: M.D. acknowledges support by the Hellenic Foundation for Research and Innovation (HFRI) under the HFRI PhD Fellowship grant (Fellowship number: 16199). D.A.P. acknowledges support by the Max Planck Society. M.O. and D.A.P. gratefully acknowledge financial support of this work by the French National Research Agency and the Deutsche Forschungsgemeinschaft (CUBISM, grant No. ANR-18 CE092_0040_01/DFG project No. 406697875), and from the France-Germany Hubert Curien Program—German Academic Exchange Service (DAAD) (Procope 2019–2020 project 42525PB/DAAD project 57445526). The authors acknowledge support from COST Action 18234 supported by European Cooperation in Science and Technology.

Data Availability Statement: Data is contained within the article or supplementary material.

Conflicts of Interest: The authors declare no conflict of interest.

References

1. Karlin, K.D.; Tyeklár, Z. *Bioinorganic Chemistry of Copper*; Springer: Dordrecht, The Netherlands, 2013; ISBN 978-94-011-6875-5.
2. Kaim, W.; Schwederski, B.; Klein, A. *Bioinorganic Chemistry: Inorganic Elements in the Chemistry of Life: An Introduction and Guide*, 2nd ed.; Inorganic Chemistry: A Wiley Series of Advanced Textbooks; Wiley: Chichester, UK, 2013; ISBN 978-0-470-97524-4.
3. Festa, R.A.; Thiele, D.J. Copper: An Essential Metal in Biology. *Curr. Biol.* **2011**, *21*, R877–R883. [[CrossRef](#)] [[PubMed](#)]
4. Solomon, E.I.; Heppner, D.E.; Johnston, E.M.; Ginsbach, J.W.; Cirera, J.; Qayyum, M.; Kieber-Emmons, M.T.; Kjaergaard, C.H.; Hadt, R.G.; Tian, L. Copper Active Sites in Biology. *Chem. Rev.* **2014**, *114*, 3659–3853. [[CrossRef](#)]
5. Belle, C.; Rammal, W.; Pierre, J. Sulfur Ligation in Copper Enzymes and Models. *J. Inorg. Biochem.* **2005**, *99*, 1929–1936. [[CrossRef](#)] [[PubMed](#)]
6. MacPherson, I.S.; Murphy, M.E.P. Type-2 Copper-Containing Enzymes. *Cell. Mol. Life Sci.* **2007**, *64*, 2887–2899. [[CrossRef](#)]
7. Pretzler, M.; Rompel, A. What Causes the Different Functionality in Type-III-Copper Enzymes? A State of the Art Perspective. *Inorg. Chim. Acta* **2018**, *481*, 25–31. [[CrossRef](#)]
8. Peisach, J.; Blumberg, W.E. Structural Implications Derived from the Analysis of Electron Paramagnetic Resonance Spectra of Natural and Artificial Copper Proteins. *Arch. Biochem. Biophys.* **1974**, *165*, 691–708. [[CrossRef](#)]
9. Solomon, E.I.; Hare, J.W.; Dooley, D.M.; Dawson, J.H.; Stephens, P.J.; Gray, H.B. Spectroscopic Studies of Stellacyanin, Plastocyanin, and Azurin. Electronic Structure of the Blue Copper Sites. *J. Am. Chem. Soc.* **1980**, *102*, 168–178. [[CrossRef](#)]
10. Gewirth, A.A.; Cohen, S.L.; Schugar, H.J.; Solomon, E.I. Spectroscopic and Theoretical Studies of the Unusual EPR Parameters of Distorted Tetrahedral Cupric Sites: Correlations to x-Ray Spectral Features of Core Levels. *Inorg. Chem.* **1987**, *26*, 1133–1146. [[CrossRef](#)]
11. Shadle, S.E.; Penner-Hahn, J.E.; Schugar, H.J.; Hedman, B.; Hodgson, K.O.; Solomon, E.I. X-Ray Absorption Spectroscopic Studies of the Blue Copper Site: Metal and Ligand K-Edge Studies to Probe the Origin of the EPR Hyperfine Splitting in Plastocyanin. *J. Am. Chem. Soc.* **1993**, *115*, 767–776. [[CrossRef](#)]
12. Andersson, K.K.; Schmidt, P.P.; Katterle, B.; Strand, K.R.; Palmer, A.E.; Lee, S.-K.; Solomon, E.I.; Gräslund, A.; Barra, A.-L. Examples of High-Frequency EPR Studies in Bioinorganic Chemistry. *J. Biol. Inorg. Chem.* **2003**, *8*, 235–247. [[CrossRef](#)]
13. de Almeida, K.J.; Rinkevicius, Z.; Hugosson, H.W.; Ferreira, A.C.; Ågren, H. Modeling of EPR Parameters of Copper(II) Aqua Complexes. *Chem. Phys.* **2007**, *332*, 176–187. [[CrossRef](#)]
14. Kaupp, M.; Bühl, M.; Malkin, V.G. (Eds.) *Calculation of NMR and EPR Parameters: Theory and Applications*, 1st ed.; Wiley: Hoboken, NJ, USA, 2004; ISBN 978-3-527-30779-1.
15. Sinnecker, S.; Neese, F. Theoretical Bioinorganic Spectroscopy. In *Atomistic Approaches in Modern Biology*; Reiher, M., Ed.; Topics in Current Chemistry; Springer: Berlin/Heidelberg, Germany, 2007; Volume 268, pp. 47–83. ISBN 978-3-540-38082-5.
16. Neese, F. Prediction of Molecular Properties and Molecular Spectroscopy with Density Functional Theory: From Fundamental Theory to Exchange-Coupling. *Coord. Chem. Rev.* **2009**, *253*, 526–563. [[CrossRef](#)]
17. Orio, M.; Pantazis, D.A. Successes, Challenges, and Opportunities for Quantum Chemistry in Understanding Metalloenzymes for Solar Fuels Research. *Chem. Commun.* **2021**, *57*, 3952–3974. [[CrossRef](#)] [[PubMed](#)]
18. Remenyi, C.; Reviakine, R.; Kaupp, M. Density Functional Study of EPR Parameters and Spin-Density Distribution of Azurin and Other Blue Copper Proteins. *J. Phys. Chem. B* **2007**, *111*, 8290–8304. [[CrossRef](#)] [[PubMed](#)]
19. Sinnecker, S.; Neese, F. QM/MM Calculations with DFT for Taking into Account Protein Effects on the EPR and Optical Spectra of Metalloproteins. Plastocyanin as a Case Study. *J. Comput. Chem.* **2006**, *27*, 1463–1475. [[CrossRef](#)]
20. Ames, W.M.; Larsen, S.C. DFT Calculations of the EPR Parameters for Cu(I) DETA Imidazole Complexes. *Phys. Chem. Chem. Phys.* **2009**, *11*, 8266. [[CrossRef](#)]
21. Ames, W.M.; Larsen, S.C. Density Functional Theory Investigation of EPR Parameters for Tetragonal Cu(II) Model Complexes with Oxygen Ligands. *J. Phys. Chem. A* **2009**, *113*, 4305–4312. [[CrossRef](#)]
22. Courtade, G.; Ciano, L.; Paradisi, A.; Lindley, P.J.; Forsberg, Z.; Sørli, M.; Wimmer, R.; Davies, G.J.; Eijsink, V.G.H.; Walton, P.H.; et al. Mechanistic Basis of Substrate–O₂ Coupling within a Chitin-Active Lytic Polysaccharide Monooxygenase: An Integrated NMR/EPR Study. *Proc. Natl. Acad. Sci. USA* **2020**, *117*, 19178–19189. [[CrossRef](#)]
23. Bissaro, B.; Streit, B.; Isaksen, I.; Eijsink, V.G.H.; Beckham, G.T.; DuBois, J.L.; Røhr, Å.K. Molecular Mechanism of the Chitinolytic Peroxygenase Reaction. *Proc. Natl. Acad. Sci. USA* **2020**, *117*, 1504–1513. [[CrossRef](#)]
24. Theibich, Y.A.; Sauer, S.P.A.; Leggio, L.L.; Hedegård, E.D. Estimating the Accuracy of Calculated Electron Paramagnetic Resonance Hyperfine Couplings for a Lytic Polysaccharide Monooxygenase. *Comput. Struct. Biotechnol. J.* **2021**, *19*, 555–567. [[CrossRef](#)]
25. Singh, S.K.; Atanasov, M.; Neese, F. Challenges in Multireference Perturbation Theory for the Calculations of the *g*-Tensor of First-Row Transition-Metal Complexes. *J. Chem. Theory Comput.* **2018**, *14*, 4662–4677. [[CrossRef](#)] [[PubMed](#)]
26. Sciortino, G.; Lubinu, G.; Maréchal, J.-D.; Garribba, E. DFT Protocol for EPR Prediction of Paramagnetic Cu(II) Complexes and Application to Protein Binding Sites. *Magnetochemistry* **2018**, *4*, 55. [[CrossRef](#)]
27. Zhou, C.; Wu, D.; Gagliardi, L.; Truhlar, D.G. Calculation of the Zeeman Effect for Transition-Metal Complexes by Multiconfiguration Pair-Density Functional Theory. *J. Chem. Theory Comput.* **2021**, *17*, 5050–5063. [[CrossRef](#)] [[PubMed](#)]
28. Ames, W.M.; Larsen, S.C. Insight into the Copper Coordination Environment in the Prion Protein through Density Functional Theory Calculations of EPR Parameters. *J. Biol. Inorg. Chem.* **2009**, *14*, 547–557. [[CrossRef](#)]

29. Kumar, S.; Sharma, R.P.; Venugopalan, P.; Witwicki, M.; Ferretti, V. Synthesis, Characterization, Single Crystal X-Ray Structure, EPR and Theoretical Studies of a New Hybrid Inorganic-Organic Compound $[\text{Cu}(\text{Hdien})_2(\text{H}_2\text{O})_2](\text{Pnb})_4 \cdot 4\text{H}_2\text{O}$ and Its Structural Comparison with Related $[\text{Cu}(\text{En})_2(\text{H}_2\text{O})_2](\text{Pnb})_2$. *J. Mol. Struct.* **2016**, *1123*, 124–132. [[CrossRef](#)]
30. Atanasov, M.; Daul, C.A.; Rohmer, M.-M.; Venkatachalam, T. A DFT Based Ligand Field Study of the EPR Spectra of Co(II) and Cu(II) Porphyrins. *Chem. Phys. Lett.* **2006**, *427*, 449–454. [[CrossRef](#)]
31. Ames, W.M.; Larsen, S.C. DFT Calculations of EPR Parameters for Copper(II)-Exchanged Zeolites Using Cluster Models. *J. Phys. Chem. A* **2010**, *114*, 589–594. [[CrossRef](#)]
32. Vancoillie, S.; Malmqvist, P.-Å.; Pierloot, K. Calculation of EPR g Tensors for Transition-Metal Complexes Based on Multiconfigurational Perturbation Theory (CASPT2). *Chem. Phys. Chem.* **2007**, *8*, 1803–1815. [[CrossRef](#)]
33. Bolvin, H. An Alternative Approach to the G-Matrix: Theory and Applications. *Chem. Eur. J. Chem. Phys.* **2006**, *7*, 1575–1589. [[CrossRef](#)]
34. Sayfutyarova, E.R.; Chan, G.K.-L. Electron Paramagnetic Resonance G-Tensors from State Interaction Spin-Orbit Coupling Density Matrix Renormalization Group. *J. Chem. Phys.* **2018**, *148*, 184103. [[CrossRef](#)]
35. Sayfutyarova, E.R.; Chan, G.K.-L. A State Interaction Spin-Orbit Coupling Density Matrix Renormalization Group Method. *J. Chem. Phys.* **2016**, *144*, 234301. [[CrossRef](#)] [[PubMed](#)]
36. Gómez-Piñero, R.J.; Pantazis, D.A.; Orio, M. Comparison of Density Functional and Correlated Wave Function Methods for the Prediction of Cu(II) Hyperfine Coupling Constants. *ChemPhysChem* **2020**, *21*, 2667–2679. [[CrossRef](#)] [[PubMed](#)]
37. Mardirossian, N.; Head-Gordon, M. Thirty Years of Density Functional Theory in Computational Chemistry: An Overview and Extensive Assessment of 200 Density Functionals. *Mol. Phys.* **2017**, *115*, 2315–2372. [[CrossRef](#)]
38. Perdew, J.P. Jacob's Ladder of Density Functional Approximations for the Exchange-Correlation Energy. In *AIP Conference Proceedings*; AIP: Antwerp, Belgium, 2001; Volume 577, pp. 1–20. [[CrossRef](#)]
39. Kaupp, M.; Reviakine, R.; Malkina, O.L.; Arbuznikov, A.; Schimmelpfennig, B.; Malkin, V.G. Calculation of Electronic G-Tensors for Transition Metal Complexes Using Hybrid Density Functionals and Atomic Meanfield Spin-Orbit Operators. *J. Comput. Chem.* **2002**, *23*, 794–803. [[CrossRef](#)] [[PubMed](#)]
40. Fritscher, J.; Hrobárik, P.; Kaupp, M. Computational Studies of Electron Paramagnetic Resonance Parameters for Paramagnetic Molybdenum Complexes. I. Method Validation on Small and Medium-Sized Systems. *J. Phys. Chem. B* **2007**, *111*, 4616–4629. [[CrossRef](#)]
41. Fritscher, J.; Hrobárik, P.; Kaupp, M. Computational Studies of EPR Parameters for Paramagnetic Molybdenum Complexes. II. Larger Mo^V Systems Relevant to Molybdenum Enzymes. *Inorg. Chem.* **2007**, *46*, 8146–8161. [[CrossRef](#)]
42. Gohr, S.; Hrobárik, P.; Repiský, M.; Komorovský, S.; Ruud, K.; Kaupp, M. Four-Component Relativistic Density Functional Theory Calculations of EPR g—and Hyperfine-Coupling Tensors Using Hybrid Functionals: Validation on Transition-Metal Complexes with Large Tensor Anisotropies and Higher-Order Spin-Orbit Effects. *J. Phys. Chem. A* **2015**, *119*, 12892–12905. [[CrossRef](#)]
43. Munzarová, M.; Kaupp, M. A Critical Validation of Density Functional and Coupled-Cluster Approaches for the Calculation of EPR Hyperfine Coupling Constants in Transition Metal Complexes. *J. Phys. Chem. A* **1999**, *103*, 9966–9983. [[CrossRef](#)]
44. Schattenberg, C.J.; Maier, T.M.; Kaupp, M. Lessons from the Spin-Polarization/Spin-Contamination Dilemma of Transition-Metal Hyperfine Couplings for the Construction of Exchange-Correlation Functionals. *J. Chem. Theory Comput.* **2018**, *14*, 5653–5672. [[CrossRef](#)]
45. Goerigk, L.; Grimme, S. Double-Hybrid Density Functionals: Double-Hybrid Density Functionals. *WIREs Comput. Mol. Sci.* **2014**, *4*, 576–600. [[CrossRef](#)]
46. Martin, J.M.L.; Santra, G. Empirical Double-Hybrid Density Functional Theory: A 'Third Way' in Between WFT and DFT. *Isr. J. Chem.* **2020**, *60*, 787–804. [[CrossRef](#)]
47. Grimme, S. Semiempirical Hybrid Density Functional with Perturbative Second-Order Correlation. *J. Chem. Phys.* **2006**, *124*, 034108. [[CrossRef](#)] [[PubMed](#)]
48. Radoń, M. Revisiting the Role of Exact Exchange in DFT Spin-State Energetics of Transition Metal Complexes. *Phys. Chem. Chem. Phys.* **2014**, *16*, 14479–14488. [[CrossRef](#)] [[PubMed](#)]
49. Pinter, B.; Chankisjijev, A.; Geerlings, P.; Harvey, J.N.; De Proft, F. Conceptual Insights into DFT Spin-State Energetics of Octahedral Transition-Metal Complexes through a Density Difference Analysis. *Chem. Eur. J.* **2018**, *24*, 5281–5292. [[CrossRef](#)]
50. Cremer, D. Density Functional Theory: Coverage of Dynamic and Non-Dynamic Electron Correlation Effects. *Mol. Phys.* **2001**, *99*, 1899–1940. [[CrossRef](#)]
51. Tran, V.A.; Neese, F. Double-Hybrid Density Functional Theory for g-Tensor Calculations Using Gauge Including Atomic Orbitals. *J. Chem. Phys.* **2020**, *153*, 054105. [[CrossRef](#)]
52. Alipour, M. How Well Can Parametrized and Parameter-Free Double-Hybrid Approximations Predict Response Properties of Hydrogen-Bonded Systems? Dipole Polarizabilities of Water Nanoclusters as a Working Model. *J. Phys. Chem. A* **2013**, *117*, 4506–4513. [[CrossRef](#)]
53. Kossmann, S.; Kirchner, B.; Neese, F. Performance of Modern Density Functional Theory for the Prediction of Hyperfine Structure: Meta-GGA and Double Hybrid Functionals. *Mol. Phys.* **2007**, *105*, 2049–2071. [[CrossRef](#)]
54. Witwicki, M.; Walencik, P.K.; Jezierska, J. How Accurate Is Density Functional Theory in Predicting Spin Density? An Insight from the Prediction of Hyperfine Coupling Constants. *J. Mol. Model.* **2020**, *26*, 10. [[CrossRef](#)]

55. Dittmer, A.; Stoychev, G.L.; Maganas, D.; Auer, A.A.; Neese, F. Computation of NMR Shielding Constants for Solids Using an Embedded Cluster Approach with DFT, Double-Hybrid DFT, and MP2. *J. Chem. Theory Comput.* **2020**, *16*, 6950–6967. [[CrossRef](#)]
56. Scholl, H.J.; Huettermann, J. ESR and ENDOR of Copper(II) Complexes with Nitrogen Donors: Probing Parameters for Prosthetic Group Modeling of Superoxide Dismutase. *J. Phys. Chem.* **1992**, *96*, 9684–9691. [[CrossRef](#)]
57. Yordanov, N.D.; Stankova, M.; Shopov, D. EPR Study of Bis(8-Quinolinethiolato) Copper(II) and Bis(8-Quinolinolato) Copper(II) Complexes. *Chem. Phys. Lett.* **1976**, *39*, 174–176. [[CrossRef](#)]
58. Kuźniarska-Biernacka, I.; Kurzak, K.; Kurzak, B.; Jezierska, J. Spectrochemical Properties of Noncubical Transition Metal Complexes in Solutions. XV. Solution Properties of Bis (Salicylideneaniline)Copper(II). *J. Solut. Chem.* **2003**, *32*, 719–741. [[CrossRef](#)]
59. Folli, A.; Ritterskamp, N.; Richards, E.; Platts, J.A.; Murphy, D.M. Probing the Structure of Copper(II)-Casiopeina Type Coordination Complexes [Cu(O-O)(N-N)]⁺ by EPR and ENDOR Spectroscopy. *J. Catal.* **2021**, *394*, 220–227. [[CrossRef](#)]
60. Uçar, İ.; Bulut, A.; Büyükgüngör, O. Synthesis, Crystal Structure, EPR and Electrochemical Studies of Copper(II) Dipicolinate Complex with 2,2'-Dipyridylamine Ligand. *J. Phys. Chem. Solids* **2007**, *68*, 2271–2277. [[CrossRef](#)]
61. Ritterskamp, N.; Sharples, K.; Richards, E.; Folli, A.; Chiesa, M.; Platts, J.A.; Murphy, D.M. Understanding the Coordination Modes of [Cu(Acac)₂(Imidazole)_{n=1,2}] Adducts by EPR, ENDOR, HYSCORE, and DFT Analysis. *Inorg. Chem.* **2017**, *56*, 11862–11875. [[CrossRef](#)] [[PubMed](#)]
62. Ali, M.A.; Mirza, A.H.; Fereday, R.J.; Butcher, R.J.; Fuller, J.M.; Drew, S.C.; Gahan, L.R.; Hanson, G.R.; Moubaraki, B.; Murray, K.S. Synthetic, EPR Spectroscopic, Magnetic and X-Ray Crystallographic Structural Studies on Copper(II) Complexes of the Tridentate N₂S Donor Ligand Formed from 6-Methyl-2-Formylpyridine and S-Methyldithiocarbamate (Hmpsme). *Inorg. Chim. Acta* **2005**, *358*, 3937–3948. [[CrossRef](#)]
63. Seena, E.B.; Kurup, M.R.P. Spectral and Structural Studies of Mono- and Binuclear Copper(II) Complexes of Salicylaldehyde N(4)-Substituted Thiosemicarbazones. *Polyhedron* **2007**, *26*, 829–836. [[CrossRef](#)]
64. West, D.X.; Salberg, M.M.; Bain, G.A.; Liberta, A.E.; Valdés-Martínez, J.; Hernández-Ortega, S. Binuclear Copper(II) Complexes of 5-Nitrosalicylaldehyde N(3)-Substituted Thiosemicarbazones. *Transit. Met. Chem.* **1996**, *21*, 206–212. [[CrossRef](#)]
65. García-Tojal, J.; García-Orad, A.; Serra, J.L.; Pizarro, J.L.; Lezama, L.; Arriortua, M.I.; Rojo, T. Synthesis and Spectroscopic Properties of Copper(II) Complexes Derived from Thiophene-2-Carbaldehyde Thiosemicarbazone. Structure and Biological Activity of [Cu(C₆H₆N₃S₂)₂]. *J. Inorg. Biochem.* **1999**, *75*, 45–54. [[CrossRef](#)]
66. Bharadwaj, P.K.; Potenza, J.A.; Schugar, H.J. Characterization of [Dimethyl N,N'-Ethylenebis(L-Cysteinato)(2-)-S,S']Copper(II), a Stable Copper(II) Aliphatic Dithiolate. *J. Am. Chem. Soc.* **1986**, *108*, 1351–1352. [[CrossRef](#)]
67. Suzuki, Y.; Fujii, S.; Tominaga, T.; Yoshimoto, T.; Yoshimura, T.; Kamada, H. The Origin of an EPR Signal Observed in Dithiocarbamate-Loaded Tissues. *Biochim. Biophys. Acta Gen. Subj.* **1997**, *1335*, 242–245. [[CrossRef](#)]
68. Glass, R.S.; Steffen, L.K.; Swanson, D.D.; Wilson, G.S.; de Gelder, R.; de Graaff, R.A.G.; Reedijk, J. Bis(Trithiacyclononane)Metal(II) Compounds and Jahn-Teller Distortions from Octahedral Geometry, Electrochemistry, Spectroscopy, and Crystal Structures of the Copper Bis(Tetrafluoroborate) Bis(Acetonitrile) Complex at 177 K and the Cadmium Bis(Tetrafluoroborate) and Copper Bis(Tetrafluoroborate) Bis(Nitromethane) Complexes at 300 K. *Inorg. Chim. Acta* **1993**, *207*, 241–252. [[CrossRef](#)]
69. Schwabe, T.; Grimme, S. Towards Chemical Accuracy for the Thermodynamics of Large Molecules: New Hybrid Density Functionals Including Non-Local Correlation Effects. *Phys. Chem. Chem. Phys.* **2006**, *8*, 4398. [[CrossRef](#)]
70. Karton, A.; Tarnopolsky, A.; Lamère, J.-F.; Schatz, G.C.; Martin, J.M.L. Highly Accurate First-Principles Benchmark Data Sets for the Parametrization and Validation of Density Functional and Other Approximate Methods. Derivation of a Robust, Generally Applicable, Double-Hybrid Functional for Thermochemistry and Thermochemical Kinetics. *J. Phys. Chem. A* **2008**, *112*, 12868–12886. [[CrossRef](#)]
71. Tarnopolsky, A.; Karton, A.; Sertchook, R.; Vuzman, D.; Martin, J.M.L. Double-Hybrid Functionals for Thermochemical Kinetics. *J. Phys. Chem. A* **2008**, *112*, 3–8. [[CrossRef](#)]
72. Brémond, É.; Sancho-García, J.C.; Pérez-Jiménez, Á.J.; Adamo, C. Communication: Double-Hybrid Functionals from Adiabatic-Connection: The QIDH Model. *J. Chem. Phys.* **2014**, *141*, 031101. [[CrossRef](#)]
73. Brémond, E.; Adamo, C. Seeking for Parameter-Free Double-Hybrid Functionals: The PBE0-DH Model. *J. Chem. Phys.* **2011**, *135*, 024106. [[CrossRef](#)]
74. Brémond, É.; Savarese, M.; Pérez-Jiménez, Á.J.; Sancho-García, J.C.; Adamo, C. Range-Separated Double-Hybrid Functional from Nonempirical Constraints. *J. Chem. Theory Comput.* **2018**, *14*, 4052–4062. [[CrossRef](#)]
75. Brémond, É.; Pérez-Jiménez, Á.J.; Sancho-García, J.C.; Adamo, C. Range-Separated Hybrid Density Functionals Made Simple. *J. Chem. Phys.* **2019**, *150*, 201102. [[CrossRef](#)]
76. Kozuch, S.; Gruzman, D.; Martin, J.M.L. DSD-BLYP: A General Purpose Double Hybrid Density Functional Including Spin Component Scaling and Dispersion Correction. *J. Phys. Chem. C* **2010**, *114*, 20801–20808. [[CrossRef](#)]
77. Kozuch, S.; Martin, J.M.L. DSD-PBEP86: In Search of the Best Double-Hybrid DFT with Spin-Component Scaled MP2 and Dispersion Corrections. *Phys. Chem. Chem. Phys.* **2011**, *13*, 20104. [[CrossRef](#)] [[PubMed](#)]
78. Iikura, H.; Tsuneda, T.; Yanai, T.; Hirao, K. A Long-Range Correction Scheme for Generalized-Gradient-Approximation Exchange Functionals. *J. Chem. Phys.* **2001**, *115*, 3540–3544. [[CrossRef](#)]
79. Yanai, T.; Tew, D.P.; Handy, N.C. A New Hybrid Exchange–Correlation Functional Using the Coulomb-Attenuating Method (CAM-B3LYP). *Chem. Phys. Lett.* **2004**, *393*, 51–57. [[CrossRef](#)]

80. Chai, J.-D.; Head-Gordon, M. Long-Range Corrected Hybrid Density Functionals with Damped Atom–Atom Dispersion Corrections. *Phys. Chem. Chem. Phys.* **2008**, *10*, 6615. [[CrossRef](#)]
81. Casanova-Páez, M.; Dardis, M.B.; Goerigk, L. Ω B2PLYP and Ω B2GPPLYP: The First Two Double-Hybrid Density Functionals with Long-Range Correction Optimized for Excitation Energies. *J. Chem. Theory Comput.* **2019**, *15*, 4735–4744. [[CrossRef](#)]
82. Casanova-Páez, M.; Goerigk, L. Time-Dependent Long-Range-Corrected Double-Hybrid Density Functionals with Spin-Component and Spin-Opposite Scaling: A Comprehensive Analysis of Singlet–Singlet and Singlet–Triplet Excitation Energies. *J. Chem. Theory Comput.* **2021**, *17*, 5165–5186. [[CrossRef](#)]
83. Chai, J.-D.; Head-Gordon, M. Long-Range Corrected Double-Hybrid Density Functionals. *J. Chem. Phys.* **2009**, *131*, 174105. [[CrossRef](#)]
84. Medvedev, M.G.; Bushmarinov, I.S.; Sun, J.; Perdew, J.P.; Lyssenko, K.A. Density Functional Theory Is Straying from the Path toward the Exact Functional. *Science* **2017**, *355*, 49–52. [[CrossRef](#)]
85. Kepp, K.P. Comment on “Density Functional Theory Is Straying from the Path toward the Exact Functional”. *Science* **2017**, *356*, 496. [[CrossRef](#)]
86. Savarese, M.; Brémond, É.; Ciofini, I.; Adamo, C. Electron Spin Densities and Density Functional Approximations: Open-Shell Polycyclic Aromatic Hydrocarbons as Case Study. *J. Chem. Theory Comput.* **2020**, *16*, 3567–3577. [[CrossRef](#)] [[PubMed](#)]
87. Sharkas, K.; Toulouse, J.; Savin, A. Double-Hybrid Density-Functional Theory Made Rigorous. *J. Chem. Phys.* **2011**, *134*, 064113. [[CrossRef](#)] [[PubMed](#)]
88. Neese, F.; Wennmo, F.; Becker, U.; Riplinger, C. The ORCA Quantum Chemistry Program Package. *J. Chem. Phys.* **2020**, *152*, 224108. [[CrossRef](#)]
89. Becke, A.D. Density-Functional Exchange–Energy Approximation with Correct Asymptotic Behavior. *Phys. Rev. A* **1988**, *38*, 3098–3100. [[CrossRef](#)] [[PubMed](#)]
90. Lee, C.; Yang, W.; Parr, R.G. Development of the Colle–Salvetti Correlation–Energy Formula into a Functional of the Electron Density. *Phys. Rev. B* **1988**, *37*, 785–789. [[CrossRef](#)]
91. Becke, A.D. A New Mixing of Hartree–Fock and Local Density-functional Theories. *J. Chem. Phys.* **1993**, *98*, 1372–1377. [[CrossRef](#)]
92. Groom, C.R.; Bruno, I.J.; Lightfoot, M.P.; Ward, S.C. The Cambridge Structural Database. *Acta Crystallogr. B Struct. Sci. Cryst. Eng. Mater.* **2016**, *72*, 171–179. [[CrossRef](#)]
93. Van Lenthe, E.; Baerends, E.J.; Snijders, J.G. Relativistic Regular Two-component Hamiltonians. *J. Chem. Phys.* **1993**, *99*, 4597–4610. [[CrossRef](#)]
94. van Lenthe, E.; Baerends, E.J.; Snijders, J.G. Relativistic Total Energy Using Regular Approximations. *J. Chem. Phys.* **1994**, *101*, 9783–9792. [[CrossRef](#)]
95. Neese, F. An Improvement of the Resolution of the Identity Approximation for the Formation of the Coulomb Matrix. *J. Comput. Chem.* **2003**, *24*, 1740–1747. [[CrossRef](#)]
96. Neese, F.; Wennmo, F.; Hansen, A.; Becker, U. Efficient, Approximate and Parallel Hartree–Fock and Hybrid DFT Calculations. A ‘Chain-of-Spheres’ Algorithm for the Hartree–Fock Exchange. *Chem. Phys.* **2009**, *356*, 98–109. [[CrossRef](#)]
97. Pantazis, D.A.; Chen, X.-Y.; Landis, C.R.; Neese, F. All-Electron Scalar Relativistic Basis Sets for Third-Row Transition Metal Atoms. *J. Chem. Theory Comput.* **2008**, *4*, 908–919. [[CrossRef](#)] [[PubMed](#)]
98. Weigend, F.; Ahlrichs, R. Balanced Basis Sets of Split Valence, Triple Zeta Valence and Quadruple Zeta Valence Quality for H to Rn: Design and Assessment of Accuracy. *Phys. Chem. Chem. Phys.* **2005**, *7*, 3297. [[CrossRef](#)] [[PubMed](#)]
99. Weigend, F. Accurate Coulomb-Fitting Basis Sets for H to Rn. *Phys. Chem. Chem. Phys.* **2006**, *8*, 1057. [[CrossRef](#)] [[PubMed](#)]
100. Adamo, C.; Barone, V. Toward Reliable Density Functional Methods without Adjustable Parameters: The PBE0 Model. *J. Chem. Phys.* **1999**, *110*, 6158–6170. [[CrossRef](#)]
101. Perdew, J.P.; Burke, K.; Ernzerhof, M. Generalized Gradient Approximation Made Simple. *Phys. Rev. Lett.* **1996**, *77*, 3865–3868. [[CrossRef](#)]
102. Heß, B.A.; Marian, C.M.; Wahlgren, U.; Gropen, O. A Mean-Field Spin-Orbit Method Applicable to Correlated Wavefunctions. *Chem. Phys. Lett.* **1996**, *251*, 365–371. [[CrossRef](#)]
103. Neese, F. Efficient and Accurate Approximations to the Molecular Spin-Orbit Coupling Operator and Their Use in Molecular *g*-Tensor Calculations. *J. Chem. Phys.* **2005**, *122*, 034107. [[CrossRef](#)]
104. Neese, F. Calculation of the Zero-Field Splitting Tensor on the Basis of Hybrid Density Functional and Hartree-Fock Theory. *J. Chem. Phys.* **2007**, *127*, 164112. [[CrossRef](#)]